Title
Solid-state electrolyte considerations for electric vehicle batteries

Journal
Sustainable Energy & Fuels, 3(7)

ISSN
2398-4902

Authors
Shen, Hao
Yi, Eongyu
Cheng, Lei
et al.

Publication Date
2019-06-25

DOI
10.1039/c9se00119k

Peer reviewed

Solid State Electrolyte Considerations for Electric Vehicle Batteries

Hao Shen,[1,2] Eongyu Yi,[1] Lei Cheng,[3] Marco Amores,[1,4] Guoying Chen,[1] Stephen Sofie[5] and Marca M. Doeff[1]

1) Energy Storage and Distributed Resources Division, Lawrence Berkeley National Laboratory, 1 Cyclotron Road, Berkeley CA 94720
2) Center for Advancing Materials Performance from the Nanoscale (CAMP-Nano), State Key Laboratory for Mechanical Behavior of Materials, Xi’an Jiaotong University, Xi’an, Shaanxi 710049 China
3) Robert Bosch LLC, Research and Technology Center, Sunnyvale, California 94085, United States
4) Department of Chemistry, Graduate School of Science, The University of Tokyo, 7-3-1, Hongo, Bunkyo-Ku, Tokyo, 113-0033, Japan
5) Department of Mechanical & Industrial Engineering, Montana State University, Bozeman, MT 59715, United States

Abstract

The recent upsurge of interest in all solid-state lithium batteries for electric vehicles is driven by a need for improved safety and higher energy densities than what are currently available from conventional lithium-ion batteries. Replacement of flammable liquid electrolytic solutions with solid electrolytes allows the use of higher energy lithium metal anodes instead of graphite, and lessens the probability of catastrophic failure, which can result in fire. Most solid-state batteries available today, however, are fabricated in small, thin film formats requiring costly vacuum deposition technologies, and suffer from low practical energy densities due to low areal capacities that restrict their use to specialty applications. In this article, we discuss the current status of solid electrolytes for solid-state lithium batteries and what is needed from a cell design and fabrication viewpoint to develop large format devices for traction applications.

Overview of Solid Electrolytes

The discoveries of fast solid ion conductors, $RbAg_4I_5$[1] and β-alumina[2] in the late 1960's ushered in the modern era of solid state ionics and stimulated development of solid state devices based on these materials. In particular, sodium/sulfur batteries with β-alumina solid electrolytes (BASE) have reached an advanced state and have been used in large scale energy storage demonstration projects.[3] The modern era of solid state ionics coincided with a period of intensified interest in and effort on lithium metal batteries. Numerous solid lithium ion conductors including polymers,[4] glasses and glass-ceramics,[5] crystalline materials,[6] and composites[7] were discovered and intensively researched from the mid to late twentieth century on. Several materials of potential interest for lithium battery applications have emerged from these studies. In the late 1980s and 1990s, polymer electrolytes based on polyethylene oxide (PEO) complexed with lithium salts such as LiTFSI (TFSI=trifluoromethanesulfonate imide) received a great deal of attention for battery applications.[8] In general, polymer electrolytes need to be heated to about 80℃ to ensure sufficient conductivity for battery operation (generally $>10^{-4}$ S/cm).[9] While this precludes their use in consumer electronics, larger scale systems such as those used for telecommunications or electric vehicles can be managed thermally and the requirement for moderate heating is not unduly burdensome. Polymer electrolytes with good mechanical properties can be easily fabricated into thin films on a large scale, making them an attractive choice for solid-state devices, and vehicles containing lithium metal polymer batteries are commercially available as of this writing (e.g., Bolloré Bluecar). Unfortunately, the rather poor oxidative stability of the PEO-based polymers restricts the choice of cathodes to $LiFePO_4$ or other low voltage materials rather than layered transition metal oxides, which operate above 3.8V vs. Li^+/Li. This means that energy densities of these systems are often lower than that of most advanced lithium ion batteries in spite of the use of lithium metal anodes.

Polymer electrolytes resemble liquid electrolyte solutions in that, unless specifically designed, they conduct both cations and anions. In fact, anions are often more mobile than cations in these systems, leading to low or even negative transference numbers.[10] Here, transference number (t_+^0) is defined as the number of moles of an ion constituent that cross a reference plane in the device when one Faraday of current is passed.[11] This definition avoids the complication of speciation in highly non-ideal liquid and polymer solutions (free cations and those bound up in positively charged complexes make a positive contribution to t_+^0, whereas those bound up in negatively charged triplets or complexes make a negative contribution). In practice this means that concentration gradients can build up in operating cells, leading to premature failure due to salt depletion or precipitation.[12] To avoid this, cells and cell components for polymer batteries must be carefully designed for the intended use. Concentration gradients may also build up in batteries with liquid electrolytic solutions,[13] but the generally faster diffusion in liquids compared to polymer hosts allows these to dissipate more rapidly.

In contrast to polymer electrolytes, ceramic and glass ionic conductors generally have fixed anionic sub-lattices, and cations are the only mobile ionic species. This selectivity confers an advantage in that concentration polarization does not occur. This also means that lower ionic conductivities can be tolerated for single ion conductors such as ceramic electrolytes than for dual ion conductors like most polymer electrolytes. For example, reference 14 indicates that cells containing electrolytes with $t_+^0=1$ are expected to outperform those with $t_+^0=0.2$, even if the conductivity is lower by one order of magnitude.

It should be noted that some ceramic and glass electrolytes actually have conductivities that approach or exceed that of liquid electrolytes at room temperature, most notably crystalline sulfides such as LGPS ($Li_{10}GeP_2S_{12}$),[15] Li_3PS_4,[16] glasses and glass-ceramics in the Li_2S-P_2S_5 system.[17] An additional advantage is that the sulfides are somewhat ductile and can be easily densified, for example, simply by uniaxial cold-pressing. The narrow voltage stability window of the sulfides[18] means that a coating layer between the cathode and the electrolyte is often needed in order to prevent reactions.[19] In addition, many sulfides are sensitive to moisture, releasing H_2S gas on contact with air or water, and thus require special handling.[20] In spite of these difficulties, one of the earliest examples of a lithium solid state micro-battery was realized with a sulfide glass.[21]

The conductivities of oxide glasses are several orders of magnitude lower than that of the corresponding sulfides, making most of them impractical for battery applications. An exception is LiPON (lithium phosphorus oxynitride).[22] Although its room temperature conductivity is only about 10^{-6} S/cm, it is generally vacuum-deposited as a very thin film in microdevices. Its wide voltage stability window and good cycling characteristics make it ideal for small batteries with lithium anodes, although the requirement for vacuum sputtering makes larger device fabrication difficult and costly.

In contrast to the glasses, there are a number of crystalline oxides and glass-ceramics that conduct lithium sufficiently well to be considered as electrolytes for lithium batteries. These include LISICON structures (LISICON=lithium superionic conductor), most notably LATP (lithium aluminum titanium phosphate). The most conductive form of LATP is a glass-ceramic[23, 24] ($\sigma_{RT}= 10^{-3}$ S/cm). LATP is readily reduced by lithium at the anode, forming Ti in the trivalent state, which makes it electronically conductive. Thus, to prevent eventual shorting of cells, an ionically conductive interlayer such as a gel or polymer electrolyte must be used between the lithium metal anode and the LATP electrolyte layer. This arrangement of lithium/gel electrolyte/LATP has been used to fabricate protected lithium electrodes (PLEs) for aqueous batteries.[25] The LATP prevents direct contact between lithium and the catholyte (which can be sulfur, oxygen, or water itself) and allows operation well outside the voltage stability window of water. So far, cycling of these systems is fairly limited, however, due to eventual formation of mossy or dendritic lithium upon plating.

Perovskites having the composition $Li_{3x}La_{2/3-x}TiO_3$; $0.06<x<0.14$ (LLTO), are fast ion conductors with room temperature bulk conductivities of up to 10^{-3} S/cm.[26] High grain boundary resistance results in a lowering of total conductivities by two orders of magnitude. As with LATP, direct contact with lithium results in reduction of Ti and induces mixed conductivity. These issues preclude the use of LLTO in batteries, although other types of devices such as sensors[27] or electrochromics[28] have been proposed.

The most technologically interesting crystalline oxides for lithium battery applications are probably those having stuffed garnet structures, particularly variants of $Li_7La_3Zr_2O_{12}$ (LLZO).[29] LLZO exists as two polymorphs, with the cubic form having three orders of magnitude greater conductivity than the tetragonal form.[30] To stabilize the cubic form at room temperature, partial aliovalent substitution is commonly used (for example, Al^{3+}[31] or Ga^{3+}[32, 33] for $3Li^+$). The conductivities of cubic Al-substituted LLZO range from about 1-8x10^{-4} S/cm,[34, 35] depending on composition, fabrication method, microstructure,[36] and other factors. Recently, even higher conductivities of over 1 mS/cm at room temperature have been reported for F-doped Ga-substituted LLZO.[37] Unlike LATP or LLTO, Al-substituted LLZO appears to passivate in contact with lithium metal,[38] forming a protective solid electrolyte interphase; thus no interlayer is required. In addition, reasonable stability is predicted for garnets in contact with 4V electrodes like

$LiCoO_{2}$,[39] and, while reaction with air (particularly if moisture is present) causes Li_2CO_3 to form,[40] simple heat treatments are effective at reversing this process.[41, 42] The lower reactivity compared to sulfides presents a considerable advantage; however, LLZO variants are notoriously more difficult to densify. Temperatures in excess of 1000℃ are often required, and lithium volatilization then may result in formation of impurities.[36,43] To compensate, excess lithium precursor may be added, but over-shooting can result in the formation of the less conductive tetragonal phase, requiring careful tuning of conditions. Figure 1 shows the sensitivity of LLZO films to sintering temperatures.[43] The amounts and types of impurities formed are also a function of component thicknesses due to variations in lithium volatilization rates (Figure 2).

While great progress has been made in the field of lithium ion conductors for solid-state batteries, it is clear that no one system, as of yet, is completely ideal or has all of the desired characteristics of high ionic conductivity, low electronic conductivity, good mechanical properties, sufficient anodic and cathodic stability, processability, low cost, and environmental friendliness needed for battery applications (Table 1).[44] What is necessary to design batteries for vehicle applications and strategies for overcoming deficiencies, particularly those utilizing garnet electrolytes, are covered in the next section.

Considerations for Cell Design

All solid-state lithium batteries in thin film formats have been studied for several decades, and have even been commercialized to a limited extent (see, for example, products made by Infinite Power Solutions). With the exception of systems utilizing polymer electrolytes (e.g, the Bluecar example mentioned above), these devices are made using vacuum deposition techniques and have small form factors. Furthermore, cathode areal capacities are low, resulting in meager energy densities. For large-scale applications such as electric vehicles, devices with thicker cathodes are needed, as well as fabrication methods that are low-cost, high throughput, and scalable.

In terms of cell design, it is instructive to consider the conventional lithium-ion battery (LIB).[45] In LIBs, cathodes are typically in the range of 20-100 μm thick, with the thicker end of that range the most desirable option for high-energy cell designs. To ensure efficient electronic pathways among active particles, electroactive materials are typically cast in composite form with conductive additives such as carbon and binder on current collectors (Al for cathodes and Cu for anodes). The binder serves to ameliorate volume changes (that can physically damage the integrity of the electrode in the extreme) associated with redox processes during charge and discharge. Approximately 25 vol.% electrolytic solution is added to the porous composite electrode to impart sufficient ionic conductivity to pass current. A porous separator wetted with electrolytic solution is sandwiched between the cathode and anode (typically graphite composite electrodes), and the assembly is contained in a casing to form the cell.

Making an analogous device using solid-state electrolyte presents some unique challenges that require both scientific and engineering solutions. One of these challenges is that it can be difficult to maintain good contact between two solids; e.g., the lithium anode and a dense separator composed of LLZO. Early iterations of Li/LLZO/Li symmetrical cells showed high interfacial impedances.[46, 47] Application of high external pressure to overcome contact resistance reduced these to an acceptable degree.[48, 49] The chemistry of the garnet phase also influences the interfacial impedance that is observed in cells; for example, Buschmann et al. observed that Ta-containing variants were superior to Al-substituted LLZO.[50] Subsequent work by Cheng et al.[40] identified the presence of Li_2CO_3 on surfaces of Al-substituted LLZO pellets as the culprit in the latter case. The Li_2CO_3 may be present as a side-product of the synthesis procedure or result from air-exposure during subsequent processing. In any case, even very small amounts, detectable only by surface-sensitive techniques such as synchrotron X-ray absorption spectroscopy (XAS) or X-ray photoelectron spectroscopy (XPS, Figure 3), can raise the interfacial impedance by nearly an order of magnitude. In reference [40], Li_2CO_3 was removed from the pellets by polishing; subsequent work has shown that carbothermal treatment,[41] incorporation of LiF during synthesis,[51] or even treatment at moderately low temperatures under inert atmosphere[42] removes or reduces the amount of Li_2CO_3, resulting in improvement. There is also a correlation between microstructure and the interfacial impedance observed in Li/LLZO/Li symmetrical cells;[52] the grain boundary chemistry of large-grained samples differs somewhat from that of small-grained samples, rendering the former more air-sensitive and more prone to forming Li_2CO_3. Figure 4 shows O K-edge soft X-ray absorption spectroscopy on pristine and air-exposed large and small-grained LLZO samples. There is relatively more Li_2CO_3 observed in the large-grained sample than in the small-grained sample after 24 hours of air exposure.

High interfacial impedances in Li/LLZO cells have also been attributed to poor wetting of the ceramic by lithium metal.[53] Atomic layer deposition of alumina coatings on dense LLZO dramatically decreases the interfacial impedance in cells. The wettability of lithiophobic surfaces is improved when a lithium-reactive coating such as gold (which alloys with lithium) is used on substrates.[54] Simple techniques such as wet chemical methods to coat garnets with ZnO[55] or even drawing on a pellet with a pencil to apply a graphite coating[56] are also effective at reducing resistance at the Li/garnet interface.

It has long been thought that solid electrolytes would enable the use of lithium metal anodes by preventing dendrite formation, a major reason for catastrophic failure of lithium batteries with liquid electrolytes, and an extreme safety concern. Monroe and Newman predicted that the use of solid polymer electrolytes with shear moduli at least twice that of lithium in cells would mechanically suppress roughening, given a Poisson's ratio similar to that of PEO.[57] The high shear moduli of garnets[58] are, however, no guarantee against failure by this mechanism, as lithium can deposit in grain boundaries or flaws in the solid electrolyte above a certain critical current density, causing cell shorting or voltage instability.[59] Figure 5 shows an optical image of a large-grained LLZO bar-shaped specimen cycled in a symmetrical cell until failure occurred and then harvested for examination. Darkening of a path between the extremely large grains is telltale evidence of intergranular lithium deposition and the likely cause of cell shorting.

The critical current density above which intergranular lithium deposition occurs is highly dependent upon the microstructure,[60] with small-grained samples showing much better behavior than large-grained ones. The increased area fraction of grain boundaries and the higher tortuosity in small grained-samples is thought to dissipate current and ameliorate the current focusing that leads to dendrite formation, although it does not prevent it entirely. In Figure 6, which shows visualizations of grain boundaries obtained from SEM images on two different samples, the small-grained sample has a grain boundary area fraction of about 32%, compared to the large-grained material, which is only 16% grain boundaries. While lithium deposition still can occur, the longer and more convoluted pathways in small-grained samples compared to larger-grained ones may delay shorting, resulting in a higher critical current density. It is also possible that the grain boundary chemistry differs in these two samples, which could affect both total ionic and electronic conductivities. A recent intriguing theory posits that the higher electronic conductivities of garnet electrolytes compared to LiPON are the cause of the more frequently observed failures of cells employing the former as the solid electrolyte.[61]

The critical current density achieved in symmetrical cells is also affected by the interfacial impedance and temperature.[62] By optimizing microstructure and minimizing area specific resistance, it is possible to cycle symmetrical Li/LLZO/Li cells reliably at current densities similar to what is used for conventional Li ion batteries.[63]

Another approach is to greatly increase the contact area between the solid electrolyte and lithium metal.[64, 65] This was recently achieved by fabricating a porous/dense/porous trilayer ceramic architecture with LLZO. Lithium metal was then infiltrated into the porous layers to form the symmetrical cell. The interfacial surface area is greatly increased compared to a planar array, not only reducing the area specific impedance to below 10 Ω-cm^2, but also allowing much higher currents to be passed. A nominal current density of 10 mA/cm^2, based on geometric area, is, in actuality, many times lower for this architecture because of the increased Li/solid electrolyte contact area.

A similar principle may be applied to the positive electrode side of the cell to allow higher areal capacities to be utilized completely under operating conditions relevant to electric vehicle applications. Transport limitations of common positive electrode materials limit the thicknesses of monolithic films that can be utilized efficiently, resulting in low practical energy densities or low power capability for solid-state batteries, as currently designed.[66, 67] LIB cathodes for electric vehicle use are typically porous composites containing active material, binder, and carbon and are infiltrated with electrolytic solution. This design ensures adequate ionic and electronic conductivity to allow full utilization of electroactive materials with typical loadings of several mAh/cm^2 when batteries are discharged at C/3 rate or higher (depending on whether they are designed for high power or high energy). Ensuring and maintaining good contact without mechanical failure[68] among the various components of a composite electrode are significant challenges for a solid-state battery, requiring special considerations for design.

For all solid-state batteries, the electrolyte is most conveniently introduced during the electrode fabrication process rather than added to a porous structure afterwards, as with LIB cathodes. Components of the electrode may be compacted or sintered together[69] to make a composite. Solid-state batteries with sulfur,[70] cobalt sulfide,[71] or vanadium sulfide cathodes, [72] where the active material has been composited with sulfide electrolyte and carbon have been successfully cycled. However, the low compressibility of garnet phases make it difficult to achieve a dense percolating network by pressing at room temperature (cold pressing), and high temperature treatments can result in unwanted reactions between the solid electrolyte and the active material.[20] It may be possible to avoid this issue by using protective coatings, or rapid heating techniques. Numerous fast sintering methods have been investigated in the LLZO and other ceramic electrolyte systems; however, these methods and their viability have not been fully explored, particularly in macro-porous structures for new solid-state battery designs. For example, spark plasma sintering (SPS),[73] has been demonstrated recently to make an all-phosphate battery, and in the densification of LLZO garnets.[74] SPS methods combine lower than traditional temperatures under typically pressured configurations to utilize extremely large pulsed currents that can facilitate internal joule heating and thus enhanced densification. Field assisted[75] and flash sintering[76, 77] use similar approaches, utilizing heat assisted with direct or alternating current to facilitate atom transport. Microwave[78, 79] and microwave-assisted[80] sintering are other rapid techniques that may be useful when applied to solid state batteries. Microwave susceptibility of the garnet structure is low and

LLZO precursors have a strong temperature dependence on susceptibility, typically requiring an external susceptor and hybrid heating approach. Cold sintering[81] is another interesting possibility that has potential to yield densification of particulates at temperatures as low as 300°C, avoiding the chemical reactions that occur during traditional sintering. The potential for glassy grain boundary phases and the incongruent dissolution of precursors that can drive stoichiometric variations can result in lower total conductivities for materials densified by this method,[82] however.

Active material and conductive additive were infiltrated into the porous component of a porous/dense bilayer structure to form a cathode in reference [83] although the need for liquid electrolytic solution on the positive electrode side to make the cell function suggests that there are still some transport limitations. All of these approaches result in highly tortuous porosity in the composite electrodes. Lowering tortuosity has been shown to improve rate capability of electrodes by reducing the length of ionic and electronic pathways.[84] A promising technique for making porous ceramics with low pore tortuosity is freeze-casting.[85] In this method, a slurry of the material of interest in a suitable solvent such as water or a low melting alcohol is frozen. If processing conditions are right, particles are excluded from the ice crystals that form, consolidating laterally from growing ice crystals to form columns. The ice is then sublimed away, and the resulting porous structure is optionally heat-treated to sinter and strengthen the particulates in the columns while retaining the large, low tortuosity pores from the sublimed ice. It has been used successfully to prepare thick electrodes for batteries,[86] [87] metal foams for solid oxide fuel cells,[88] and many other materials.[89] Porosities and pore sizes and shapes can be varied over a wide range by adjusting formulations, temperature, and other parameters.

Examples of freeze-cast LLZO from our laboratories are shown in Figure 7. The images on the top and bottom left show LLZO scaffolds made using tert-butyl alcohol (TBA) as the solvent. The porosities and pore sizes vary due to the different processing temperatures (-20°C for the top one, giving 71% porosity with an average pore size of 52 μm, and -50°C for the bottom, giving 61% porosity with an average pore size of 22.5 μm). The low tortuosity, which is close to one, is evident from the images. Infiltration of NMC ($LiNi_{0.6}Mn_{0.2}Co_{0.2}O_2$) and polymer (either polyaniline or polyvinylidene fluoride (PVdF), shown at the top and bottom right of Figure 7, respectively) can easily be achieved via capillary action, due to the large pores and low tortuosity. A conducting polymer such as polyaniline provides electronic conductivity and acts as a binder, which may be used to replace both carbon and PVdF. The conductivity of these polymers can reach 10^3-10^4 S/cm, and their unique chain-like morphology allows them to provide better conducting networks among the infiltrated active particles.[90]

A variant of the freeze-casting method is freeze tape-casting (FTC),[88, 91] which is scalable and ideal for making relatively thin components, ranging from as low as 5 μm to several mm thick, suitable for batteries (Figure 8). For the ~100 μm thin scaffolds targeted for battery applications, the use of water is preferable to organic solvents, both due to its environmental friendliness and for practical reasons (water has less tendency to evaporate prematurely during FTC processing). Images of typical green body LLZO tapes produced by aqueous FTC processing are presented in Figure 9. A comparison to Figure 7 shows the very different pore shapes obtained when processing in water compared to TBA; the pores in the water-processed samples are more slit-like. Differences in the crystal growth characteristics of the solvents[85] as well as experimental conditions, account for this variation. It is not clear, at this point in time, what pore sizes and shapes are ideal for fabrication of the scaffolds for composite electrodes. Pores need to be large enough and have sufficient connectivity to enable infiltration, but intimate contact among all components is necessary to enable ionic and electronic transport throughout the structure,[45] and volume changes and strain associated with redox processes need to be accommodated.[68] Some future work in this lab will be directed towards understanding how performance and mechanical properties (ease of handling) are tied to porosity (including the total pore volume, the pore size, the pore morphology, and pore wall thickness which are all tailorable through FTC) in the scaffolds.

Another challenge associated with device design is the need to minimize the amount of LLZO used both in the electrodes and in the electrolyte layer, due to its heaviness (density ~5.1 g/cm^3). There is also a significant energy density penalty if the separator layer exceeds a thickness of about 20 μm.[92] Separators for LIBs range in thickness from about 12-40 μm, but the polymers from which they are made are significantly less dense than LLZO. Reducing the thickness of LLZO separators below 20 μm would be desirable from a specific energy perspective, but requirements for high density (as close to theoretical as possible) and absence of defects become even more stringent. This also poses a difficult engineering challenge for cell assembly. A free-standing dense and brittle electrolyte layer less than 20 μm thick is unlikely to survive the assembly process to create an intimate solid-solid interface with electrode with reasonable interfacial impedance. However, if supported on a porous scaffold, a thinner electrolyte layer could be handled with more tolerance, making it easier for processing. The porous layers can then be made up of as little LLZO as is practicable, which is important from an energy density point of view, particularly for trilayers.. The guideline of 25 vol.% electrolyte in composite cathodes for LIBs is a useful starting point (corresponding to 75 vol.% porosity for LLZO scaffolds); higher porosities than that may be needed to achieve specific energy goals, again because liquid electrolytic solutions are less dense than LLZO. LLZO scaffolds with very high porosities may tend to be fragile, although incorporating them with dense layers in bilayer or trilayer structures should improve the overall mechanical stability. Images of trilayer structures fabricated in our laboratory, which approach these high energy density goals, are presented in Figure 10.

Finally, the amount (inventory) of lithium in the cell must be strictly limited to only a small excess to achieve the desired high energy densities. Using 20% excess lithium in a solid-state device would result in a practical energy density of about 750 Wh/L on the pack level, compared to about 250 Wh/L for a typical LIB (specific energies are about 150 Wh/kg for the LIB vs. 250 Wh/kg for the lithium metal battery). [93] This would correspond to lithium foil about 20 μm thick for an areal capacity of about 4 mAh/cm^2, and requires achievement of a coulombic efficiency of 99.98% to cycle 80% of the capacity 1000 times. An advantage to LLZO, compared to liquid electrolytes and many other solid electrolytes, is its low reactivity with respect to reduction by lithium.[29, 94] A recent *in situ* microscopy study of Al substituted LLZO shows that a tetragonal LLZO interphase a few nanometers thick forms upon contact with lithium. This thin layer essentially passivates the surface and functions as a solid electrolyte interphase. If this interphase is maintained intact upon cycling, it should allow efficient plating and stripping of lithium.

Conclusions

A brief survey of several classes of solid electrolytes for lithium batteries is presented. All solid-state lithium batteries utilizing polymer electrolytes are currently utilized in electric vehicles, but their limitations mean that energy densities are lower than state-of-the-art lithium ion batteries. Ceramic or glass electrolytes have been incorporated into small lithium batteries having thin film configurations, but the vacuum deposition processes used for fabrication are costly and not easily scalable. To achieve cost, energy density, and performance goals for electric vehicles, these devices need to be redesigned to incorporate thick (~ 100 μm) composite cathodes, using low-cost manufacturing processes. The challenges here are considerable, because intimate contact among all components of the cathode (ionic conductor, electronic conductor, and active material) must be maintained throughout the charge and discharge processes. Freeze tape-casting (FTC) to make scaffolds of an ion-conducting ceramic like LLZO, which have low tortuosity pores that can be infiltrated with other components of the cathode, holds considerable promise in this regard. It is possible to combine these scaffolds with a thin, dense LLZO layer to form a bilayer structure, to which a planar lithium anode would be added to make a cell. By modifying the Li foil/dense layer interface, lithium can be reliably stripped and plated at moderate current densities without failure. By incorporating lithium into a second porous scaffold in a trilayer (porous/dense/porous) configuration, it is possible to increase the critical current density further, to the rates needed for electric vehicle operation. However, these devices need to be designed to minimize the amount of ceramic conductor as much as possible so that specific energy is not unduly compromised.

Materials and Methods

For Figure 5, Al-substituted LLZO was synthesized and processed into pellets as described in reference 36. For the freeze casting and freeze tape-casting experiments, a commercial source of Al-substituted LLZO was used (Ampcera LLZO nanopowder, MSE Supplies). NMC cathode powders for infiltration were obtained from Umicore.

Freeze casting experiments were carried out using a commercial research scale freeze tape-caster (GLA-RC2, Glacigen) was used to prepare thin porous LLZO tapes as follows. LLZO, Li_2CO_3 (Sigma-Aldrich), polyacrylic acid dispersant (Sigma Aldrich), VANZAN thickener (Xanthan gum, Vanderbilt Minerals), and DI water at selected weight ratios were ball-milled for 3-6 h. The slurry was then transferred to a Teflon beaker and acrylic latex emulsion binder (Duramax, Rohm & Hass) was mixed in by magnetic stirring for 30 min. The resulting slurry was cast onto a Mylar sheet using a doctor blade. The cast slurry was slowly pulled onto the freezing bed held at -11 °C to obtain desired microstructures. Ice was removed by freeze drying the samples under vacuum at 0.1 mbar (FreeZone Freeze Dryer, Labconco). Dense LLZO tapes were prepared using a modification of the procedure outlined in reference [43] and incorporated into trilayer structures. Further details of the freeze tape casting process and the trilayer processing will be discussed in our future publications.

Scanning electron microscopy was performed on selected samples using either a JEOL JSM-7500F instrument or a Hitachi TM-1000 tabletop microscope in secondary electron imaging (SEI) mode.

Acknowledgments

This work was supported by the Assistant Secretary for Energy Efficiency and Renewable Energy, Office of Vehicle Technologies of the U.S. Department of Energy under Contract No. DE-AC02-05CH11231. H.S. would like to thank the China Scholarships Council (NO.201606280062, 2016.9 ~ 2017.8) and ALS Doctoral Fellowship in Residence (2017.10 ~ 2018.9) for financial support.

References

1. J. N. Bradley and P. D. Greene, *Trans. Faraday Soc.*, 1967, **63**, 424-430.
2. Y.-F. Y. Yao and J. T. Kummer, *J. Inorg. Nucl. Chem.*, 1967, **29**, 2453-2473.
3. K. B. Hueso, M. Armand and T. Rojo, *Energy & Environ. Sci.*, 2013, **6**, 734.
4. J. W. Fergus, *J. Power Sources*, 2010, **195**, 4554-4569.
5. T. Minami, A. Hayashi and M. Tatsumisago, *Solid State Ionics*, 2006, **177**, 2715-2720.
6. P. Knauth, *Solid State Ionics*, 2009, **180**, 911-916.
7. N. F. Uvarov, *J. Solid State Electrochem.*, 2008, **15**, 367-389.
8. K. Xu, *Chem. Rev.*, 2004, **104**, 4303-4417.
9. L. Edman and M. Doeff, *Solid State Ionics*, 2003, **158**, 177-186.
10. Y. Ma, M. Doyle, T. F. Fuller, M. M. Doeff, L. C. D. Jonghe and J. Newman, *J. Electrochem. Soc.*, 1995, **142**, 1859-1868.
11. A. Ferry, M. M. Doeff and L. C. D. Jonghe, *Electrochim. Acta*, 1998, **43**, 1387-1395.
12. M. M. Doeff, A. Ferry, Y. Ma, L. Ding and L. C. D. Jonghe, *J. Electrochem. Soc.,* 1997, **144**, L20-22.
13. R. A. Robinson and R. H. Stokes, *Electrolyte Solutions*, Butterworths, London, second edn., 1959.

14. M. Doyle, T. F. Fuller and J. Newman, *Electrochim. Acta*, 1994, **39**, 2073-2081.
15. N. Kamaya, K. Homma, Y. Yamakawa, M. Hirayama, R. Kanno, M. Yonemura, T. Kamiyama, Y. Kato, S. Hama, K. Kawamoto and A. Mitsui, *Nature Mater.*, 2011, **10**, 682-686.
16. L. L. Baranowski, C. M. Heveran, V. L. Ferguson and C. R. Stoldt, *ACS Appl. Mater. & Interfaces*, 2016, **8**, 29573-29579.
17. Y. Seino, T. Ota, K. Takada, A. Hayashi and M. Tatsumisago, *Energy Environ. Sci.*, 2014, **7**, 627-631.
18. R. Koerver, I. Aygün, T. Leichtweiß, C. Dietrich, W. Zhang, J. O. Binder, P. Hartmann, W. G. Zeier and J. Janek, *Chem. Mater.*, 2017, **29**, 5574-5582.
19. Y. Tian, T. Shi, W. D. Richards, J. Li, J. C. Kim, S.-H. Bo and G. Ceder, *Energy & Environ. Sci.*, 2017, **10**, 1150-1166.
20. K. Kerman, A. Luntz, V. Viswanathan, Y.-M. Chiang and Z. Chen, *J. Electrochem. Soc.*, 2017, **164**, A1731-A1744.
21. S. D. Jones and J. R. Akridge, *J. Power Sources*, 1993, **43-44**, 505-513.
22. X. Yu, J. B. Bates, G. E. Jellison and F. X. Hart, *J. Electrochem. Soc.*, 1997, **144**, 524-532.
23. B. V. R. Chowdari, G. V. S. Rao and G. Y. H. Lee, *Solid State Ionics*, 2000, **136-137**, 1067-1075.
24. J. Fu, *J. Am. Ceram. Soc.*, 1997, **80**, 1901-1903.
25. S. Visco, E. Nimon and B. Katz, 2007, **U.S. Patent 7,282,296**.
26. C. Ma, K. Chen, C. Liang, C.-W. Nan, R. Ishikawa, K. More and M. Chi, *Energy & Environ Sci.*, 2014, **7**, 1638.
27. C. Bohnke, H. Duroy and J. L. Fourquet, *Sensors and Actuators B: Chemical*, 2003, **89**, 240-247.
28. O. Bohnke, *Solid State Ionics*, 2008, **179**, 9-15.
29. R. Murugan, V. Thangadurai and W. Weppner, *Angew. Chemie*, 2007, **46**, 7778-7781.
30. E. J. Cussen, *J. Mater. Chem.*, 2010, **20**, 5167.
31. C. A. Geiger, E. Alekseev, B. Lazic, M. Fisch, T. Armbruster, R. Langner, M. Fechtelkord, N. Kim, T. Pettke and W. Weppner, *Inorg. Chem.*, 2011, **50**, 1089-1097.
32. D. Rettenwander, C. A. Geiger, M. Tribus, P. Tropper and G. Amthauer, *Inorg. Chem.*, 2014, **53**, 6264-6269.
33. S. Afyon, F. Krumeich and J. L. M. Rupp, *J. Mater. Chem. A*, 2015, **3**, 18636-18648.
34. S. Ramakumar, C. Deviannapoorani, L. Dhivya, L. S. Shankar and R. Murugan, *Prog. Mater. Sci.*, 2017, **88**, 325-411.
35. A. Wachter-Welzl, J. Kirowitz, R. Wagner, S. Smetaczek, G. C. Brunauer, M. Bonta, D. Rettenwander, S. Taibl, A. Limbeck, G. Amthauer and J. Fleig, *Solid State Ionics*, 2018, **319**, 203-208.

36. L. Cheng, J. S. Park, H. Hou, V. Zorba, G. Chen, T. Richardson, J. Cabana, R. Russo and M. Doeff, *J. Mater. Chem. A*, 2014, **2**, 172-181.
37. Y. Lu, X. Meng, J. A. Alonso, M. T. Fernandez-Diaz and C. Sun, *ACS Applied Mater. & Interfaces*, 2019, **11**, 2042-2049.
38. C. Ma, Y. Cheng, K. Yin, J. Luo, A. Sharafi, J. Sakamoto, J. Li, K. L. More, N. J. Dudney and M. Chi, *Nano Lett.*, 2016, **16**, 7030-7036.
39. L. J. Miara, W. D. Richards, Y. E. Wang and G. Ceder, *Chem. Mater.*, 2015, **27**, 4040-4047.
40. L. Cheng, E. J. Crumlin, W. Chen, R. Qiao, H. Hou, S. Franz Lux, V. Zorba, R. Russo, R. Kostecki, Z. Liu, K. Persson, W. Yang, J. Cabana, T. Richardson, G. Chen and M. Doeff, *Phys. Chem. Chem. Phys.*, 2014, **16**, 18294-18300.
41. Y. Li, X. Chen, A. Dolocan, Z. Cui, S. Xin, L. Xue, H. Xu, K. Park and J. B. Goodenough, *J. Amer. Chem. Soc.*, 2018, **140**, 6448-6455.
42. L. Cheng, M. Liu, R. Davis, A. Mehta, H. Xin, F. Lin, K. A. Persson, G. Chen, E. J. Crumlin and M. Doeff, *ACS Appl. Energy Mater.*, 2018, DOI: 10.1021/acsaem.8b01723
43. E. Yi, W. Wang, J. Kieffer and R. M. Laine, *J. Mater. Chem. A*, 2016, **4**, 12947-12954.
44. C. Sun, J. Liu, Y. Gong, D. P. Wilkinson and J. Zhang, *Nano Energy*, 2017, **33**, 363-386.
45. J. Janek and W. G. Zeier, *Nature Energy*, 2016, **1**, 16141.
46. H. Buschmann, J. Dolle, S. Berendts, A. Kuhn, P. Bottke, M. Wilkening, P. Heitjans, A. Senyshyn, H. Ehrenberg, A. Lotnyk, V. Duppel, L. Kienle and J. Janek, *Phys. Chem. Chem. Phys.*, 2011, **13**, 19378-19392.
47. H. El Shinawi and J. Janek, *J. Power Sources*, 2013, **225**, 13-19.
48. K. Ishiguro, Y. Nakata, M. Matsui, I. Uechi, Y. Takeda, O. Yamamoto and N. Imanishi, *J. Electrochem. Soc.*, 2013, **160**, A1690-A1693.
49. K. Ishiguro, H. Nemori, S. Sunahiro, Y. Nakata, R. Sudo, M. Matsui, Y. Takeda, O. Yamomoto and N. Imanishi, *J. Electrochem. Soc.*, 2014, **161**, A668-A674.
50. H. Buschmann, S. Berendts, B. Mogwitz and J. Janek, *J. Power Sources*, 2012, **206**, 236-244.
51. Y. Li, B. Xu, H. Xu, H. Duan, X. Lu, S. Xin, W. Zhou, L. Xue, G. Fu, A. Manthiram and J. B. Goodenough, *Angew. Chemie*, 2017, **56**, 753-756.
52. L. Cheng, C. H. Wu, A. Jarry, W. Chen, Y. Ye, J. Zhu, R. Kostecki, K. Persson, J. Guo, M. Salmeron, G. Chen and M. Doeff, *ACS Appl. Mater. & interfaces*, 2015, **7**, 17649-17655.
53. X. Han, Y. Gong, K. K. Fu, X. He, G. T. Hitz, J. Dai, A. Pearse, B. Liu, H. Wang, G. Rubloff, Y. Mo, V. Thangadurai, E. D. Wachsman and L. Hu, *Nature Mater.*, 2017, **16**, 572-579.

54. J. Wang, H. Wang, J. Xie, A. Yang, A. Pei, C.-L. Wu, F. Shi, Y. Liu, D. Lin, Y. Gong and Y. Cui, *Energy Storage Materials*, 2018, **14**, 345-350.
55. C. Zhou, A. J. Samson, K. Hofstetter and V. Thangadurai, *Sustainable Energy & Fuels*, 2018, DOI: 10.1039/c8se00234g.
56. Y. Shao, H. Wang, Z. Gong, D. Wang, B. Zheng, J. Zhu, Y. Lu, Y.-S. Hu, X. Guo, H. Li, X. Huang, Y. Yang, C.-W. Nan and L. Chen, *ACS Energy Letters*, 2018, **3**, 1212-1218.
57. C. Monroe and J. Newman, *J. Electrochem. Soc.*, 2005, **152**, A396.
58. S. Yu, R. D. Schmidt, R. Garcia-Mendez, E. Herbert, N. J. Dudney, J. B. Wolfenstine, J. Sakamoto and D. J. Siegel, *Chem. Mater.*, 2016, **28**, 197-206.
59. E. J. Cheng, A. Sharafi and J. Sakamoto, *Electrochim. Acta*, 2017, **223**, 85-91.
60. L. Cheng, W. Chen, M. Kunz, K. Persson, N. Tamura, G. Chen and M. Doeff, *ACS Applied Materials & Interfaces*, 2015, **7**, 2073-2081.
61. F. Han, A. S. Westover, J. Yue, X. Fan, F. Wang, M. Chi, D. N. Leonard, N. J. Dudney, H. Wang and C. Wang, *Nature Energy*, 2019, **4**, 187-196.
62. A. Sharafi, H. M. Meyer, J. Nanda, J. Wolfenstine and J. Sakamoto, *J. Power Sources*, 2016, **302**, 135-139.
63. N. J. Taylor, S. Stangeland-Molo, C. G. Haslam, A. Sharafi, T. Thompson, M. Wang, R. Garcia-Mendez and J. Sakamoto, *J. Power Sources*, 2018, **396**, 314-318.
64. G. T. Hitz, D. W. McOwen, L. Zhang, Z. Ma, Z. Fu, Y. Wen, Y. Gong, J. Dai, T. R. Hamann, L. Hu and E. D. Wachsman, *Mater. Today*, 2018, DOI: 10.1016/j.mattod.2018.04.004.
65. D. W. McOwen, S. Xu, Y. Gong, Y. Wen, G. L. Godbey, J. E. Gritton, T. R. Hamann, J. Dai, G. T. Hitz, L. Hu and E. D. Wachsman, *Adv. Materials*, 2018, **30**, e1707132.
66. J. Li, C. Ma, M. Chi, C. Liang and N. J. Dudney, *Adv. Energy Mater.*, 2015, **5**, 1401408.
67. J. B. Bates, N. J. Dudney, B. Neudecker, A. Ueda and C. D. Evans, *Solid State Ionics*, 2000, **135**, 33-45.
68. R. Koerver, W. Zhang, L. de Biasi, S. Schweidler, A. O. Kondrakov, S. Kolling, T. Brezesinski, P. Hartmann, W. G. Zeier and J. Janek, *Energy & Environ. Sci.* 2018, **11**, 2142-2158.
69. J. Schnell, T. Günther, T. Knoche, C. Vieider, L. Köhler, A. Just, M. Keller, S. Passerini and G. Reinhart, *J. Power Sources*, 2018, **382**, 160-175.
70. X. Yao, N. Huang, F. Han, Q. Zhang, H. Wan, J. P. Mwizerwa, C. Wang and X. Xu, *Adv. Energy Mater.*, 2017, **7**, 1602923.
71. X. Yao, D. Liu, C. Wang, P. Long, G. Peng, Y. S. Hu, H. Li, L. Chen and X. Xu, *Nano Lett.*, 2016, **16**, 7148-7154.

72. Q. Zhang, H. Wan, G. Liu, Z. Ding, J. P. Mwizerwa and X. Yao, *Nano Energy*, 2019, **57**, 771-782.
73. A. Aboulaich, R. Bouchet, G. Delaizir, V. Seznec, L. Tortet, M. Morcrette, P. Rozier, J.-M. Tarascon, V. Viallet and M. Dollé, *Adv. Energy Mater.* 2011, **1**, 179-183.
74. S.-W. Baek, J.-M. Lee, T. Y. Kim, M.-S. Song and Y. Park, *J. Power Sources*, 2014, **249**, 197-206.
75. Y. Zhang, F. Chen, R. Tu, Q. Shen and L. Zhang, *J. Power Sources*, 2014, **268**, 960-964.
76. M. Cologna, B. Rashkova and R. Raj, *J. Am. Ceram. Soc.*, 2010, **93**, 3556-3559.
77. M. Yu, S. Grasso, R. McKinnon, T. Saunders and M. J. Reece, *Adv. Appl. Ceram.,* 2016, **116**, 24-60.
78. S. Das, A. K. Mukhopadhyay, S. Datta and D. Basu, *Bull. Mater. Sci.*, 2009, **32**, 1-13.
79. X. Lu and D. Yang, *J. Inorg. Organometal. Polym. Mater.*, 2018, **28**, 2023-2027.
80. M. Amores, T. E. Ashton, P. J. Baker, E. J. Cussen and S. A. Corr, *J. Mater. Chem. A*, 2016, **4**, 1729-1736.
81. J. Guo, H. Guo, A. L. Baker, M. T. Lanagan, E. R. Kupp, G. L. Messing and C. A. Randall, *Angew. Chemie*, 2016, **55**, 11457-11461.
82. Y. Liu, Q. Sun, D. Wang, K. Adair, J. Liang and X. Sun, *J. Power Sources*, 2018, **393**, 193-203.
83. K. Fu, Y. Gong, G. T. Hitz, D. W. McOwen, Y. Li, S. Xu, Y. Wen, L. Zhang, C. Wang, G. Pastel, J. Dai, B. Liu, H. Xie, Y. Yao, E. D. Wachsman and L. Hu, *Energy & Environ. Sci.*, 2017, **10**, 1568-1575.
84. Y. Kim, A. Drews, R. Chandrasekaran, T. Miller and J. Sakamoto, *Ionics*, 2018, DOI: 10.1007/s11581-018-2502-x.
85. S. Deville, *Adv. Eng. Mater.*, 2008, **10**, 155-169.
86. S. Behr, R. Amin, Y.-M. Chiang and A. P. Tomsia, *Process Engineering*, 2015, **92**, E39-E43.
87. M. A. Ghadkolai, S. Creager, J. Nanda and R. K. Bordia, *J. Electrochem. Soc.*, 2017, **164**, A2603-A2610.
88. D. Driscoll, A. J. Weisenstein and S. W. Sofie, *Mater. Lett.*, 2011, **65**, 3433-3435.
89. K. L. Scotti and D. C. Dunand, *Prog. Mater. Sci.*, 2018, **94**, 243-305.
90. R. Menon, C. O. Yoon, D. Moses and A. J. Heeger, *Handbook of Conducting Polymers, 2nd edition*, Marcel Dekker, New York, 1998.
91. S. W. Sofie, *J. Amer. Ceram. Soc.*, 2007, **90**, 2024-2031.
92. ARPA-E, *Integration and Optimization of Novel Ion Conducting Solids (Ionics)*, 2016, **Funding Opportunity Announcement DE-FOA-0001478**.

93. P. Albertus, S. Babinec, S. Litzelman and A. Newman, *Nature Energy*, 2017, **3**, 16-21.
94. M. Kotobuki, H. Munakata, K. Kanamura, Y. Sato and T. Yoshida, *J. Electrochem. Soc.*, 2010, **157**, A1076.

Figure Captions

Figure 1. SEM fracture surface images of films sintered at (a) and (b) 1080°, (c) and (d) 1090℃, (e) and (f) 1100℃. (g) XRD patterns of sintered LLZO films. Reproduced from Ref. 42 with permission from The Royal Society of Chemistry.

.**Figure 2.** Microstructure and phase purity dependence on LLZO green film thickness after sintering at 1090℃. SEM fracture surface images of (a) 22 μm (b) 45 μm and (c) 73 μm thick green films. (d) Surface/volume ratio plot. (e) Phase compositions as a function of green film thicknesses. Reproduced from Ref. 42 with permission from The Royal Society of Chemistry.

Figure 3. (a) C1s, La 4d, Zr 3d, and Li 1s XPS data collected from LLZO pellets polished under Ar (top, in blue) or exposed to air (bottom, in red). The absence of La and Zr signals in the latter suggest that Li_2CO_3 coverage is greater than 3 nm thick. Reproduced from Ref. 39 with permission from the PCCP Owner Societies.

Figure 4. O K-edge soft XAS spectra of a pristine large-grained LLZO pellet (P_LLZO_L), small and large-grained LLZO pellets exposed to air for 24 hours (E_LLZO_S24h and E_LLZO_L24h and Li_2CO_3 in (a) total

electron yield (TEY) mode, probing approximately 10 nm into the samples and (b) total fluorescence yield (TFY) mode, probing about 100 nm into the samples. The relative amounts of Li_2CO_3 in yellow compared to lattice oxygen in purple are shown in the expansion of the E_LLZO_S24h and E_LLZO_L24h TFY spectra (c). Reprinted with permission from Ref. 50, Copyright 2015 American Chemical Society.

Figure 5. Optical image of a LLZO pellet harvested from a symmetrical cell cycled until failure. The bar corresponds to 300 μm. The darkening along a path between the large grains is evidence of lithium deposition in grain boundaries.

Figure 6. (a) and (b) scanning electron micrographs of small and large-grained LLZO samples, and visualizations of grain boundaries. Reprinted with permission from Ref. 58. Copyright 2015 American Chemical Society.

Figure 7. Scanning electron micrographs of (left, top and bottom) freeze-cast LLZO scaffolds processed at -20°C (top) or -50°C (bottom), and (top, right) a large pore infiltrated with NMC particles and polyaniline, and (bottom, right), smaller pores infiltrated with NMC and PVdF. Bars correspond to 200 μm except for bottom right, where it corresponds to 100 μm.

Figure 8. Schematic of a freeze tape casting experiment.

Figure 9. SEM images of a FTC LLZO scaffold processed in water. Topmost images show the top of the scaffolds, and bottom images show the fracture surface cross-sections.

Figure 10. SEM images of a trilayer LLZO structure with two highly porous layers and a thin dense layer in the middle. Two magnifications are shown in left and right.

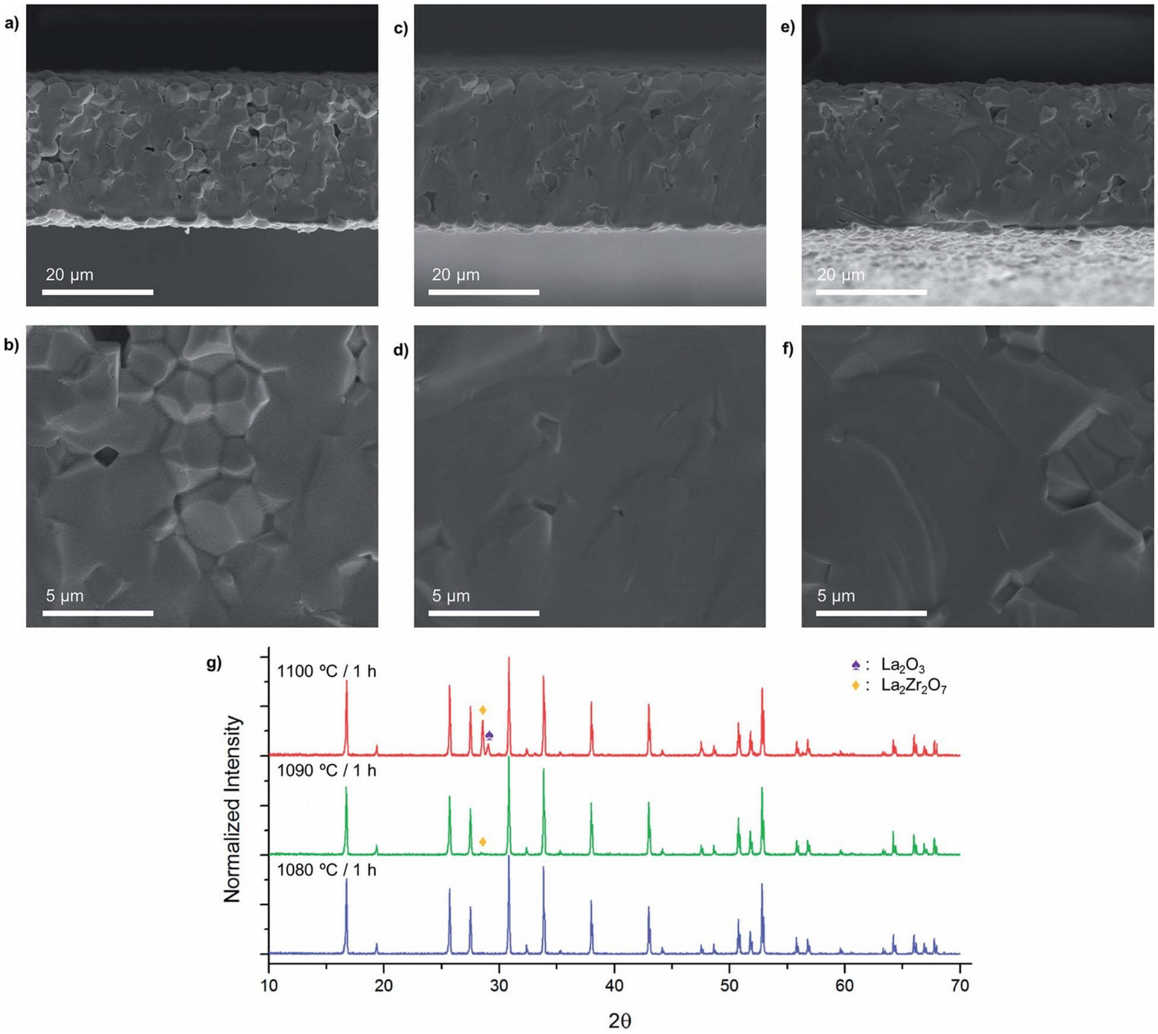
a)
20 µm
b)
5 µm
c)
20 µm
d)
5 µm
e)
20 µm
f)
5 µm
g)
1100 ºC / 1 h
1090 ºC / 1 h
1080 ºC / 1 h
♠ : La_2O_3
♦ : $La_2Zr_2O_7$
Normalized Intensity
10
20
30
40
50
60
70
2θ

Figure 1

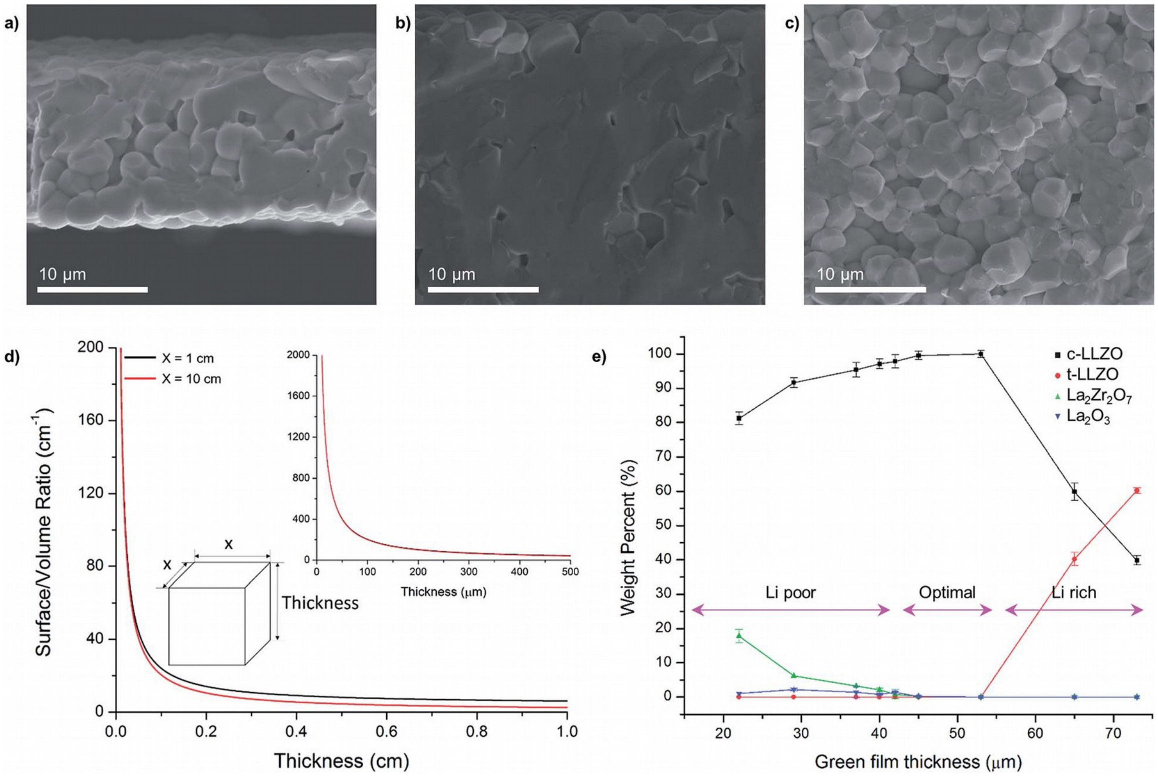
a)
10 μm
b)
10 μm
c)
10 μm
d)
X = 1 cm
X = 10 cm
Surface/Volume Ratio (cm^{-1})
200
160
120
80
40
0
0.0
0.2
0.4
0.6
0.8
1.0
Thickness (cm)
X
X
Thickness
2000
1600
1200
800
400
0
0
100
200
300
400
500
Thickness (μm)
e)
c-LLZO
t-LLZO
$La_2Zr_2O_7$
La_2O_3
Weight Percent (%)
100
90
80
70
60
50
40
30
20
10
0
Li poor
Optimal
Li rich
20
30
40
50
60
70
Green film thickness (μm)

Figure 2

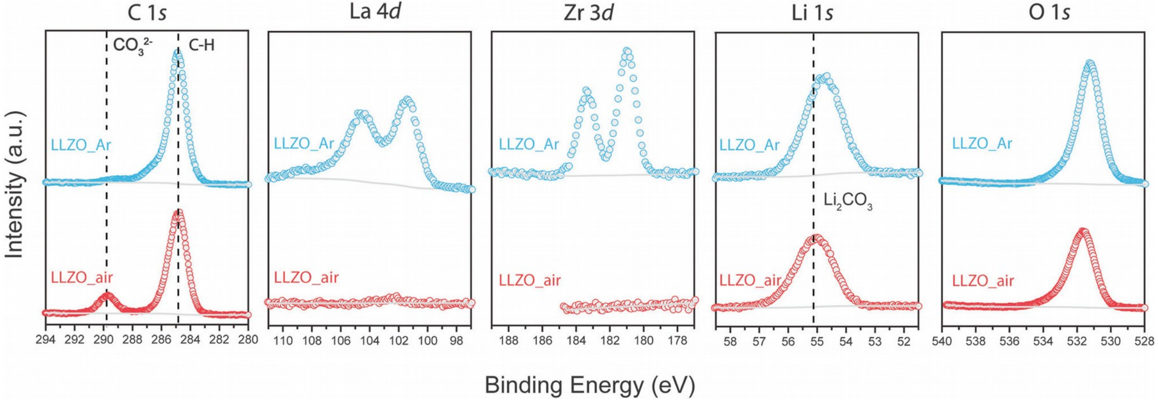
C 1s
La 4d
Zr 3d
Li 1s
O 1s
Intensity (a.u.)
CO_3^{2-}
C-H
Li_2CO_3
LLZO_Ar
LLZO_air
294 292 290 288 286 284 282 280
110 108 106 104 102 100 98
188 186 184 182 180 178
58 57 56 55 54 53 52
540 538 536 534 532 530 528
Binding Energy (eV)

Figure 3

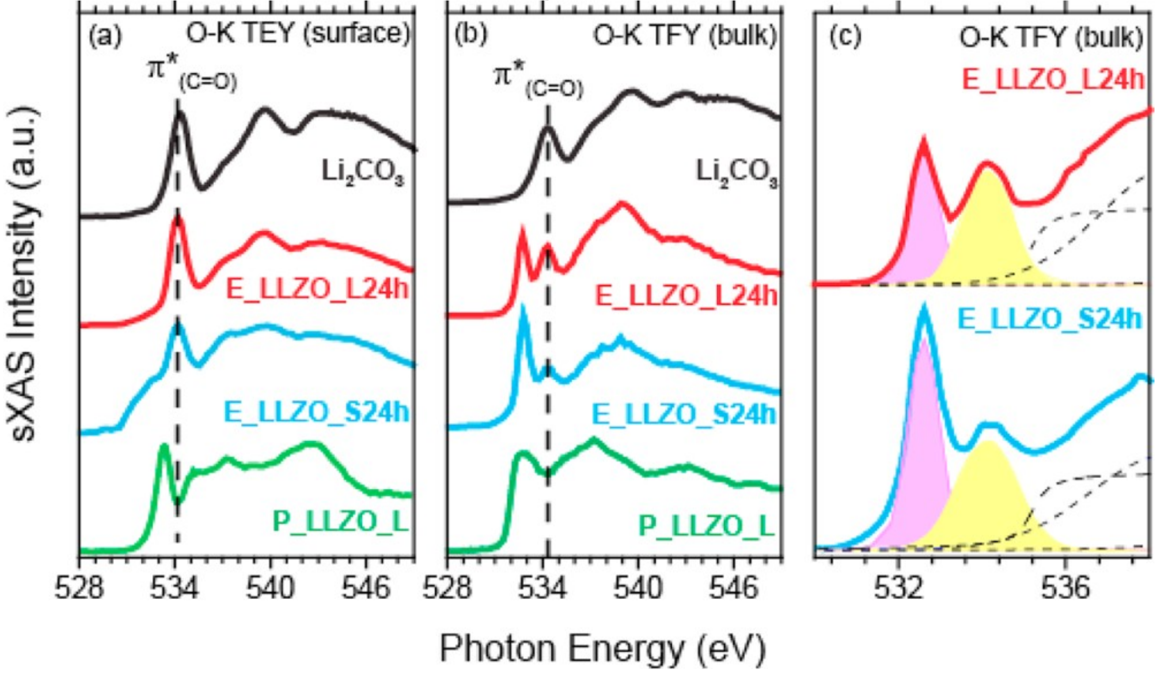

(a)
O-K TEY (surface)
π*(C=O)
Li2CO3
E_LLZO_L24h
E_LLZO_S24h
P_LLZO_L
(b)
O-K TFY (bulk)
π*(C=O)
Li2CO3
E_LLZO_L24h
E_LLZO_S24h
P_LLZO_L
(c)
O-K TFY (bulk)
E_LLZO_L24h
E_LLZO_S24h
sXAS Intensity (a.u.)
528
534
540
546
528
534
540
546
532
536
Photon Energy (eV)

Figure 4

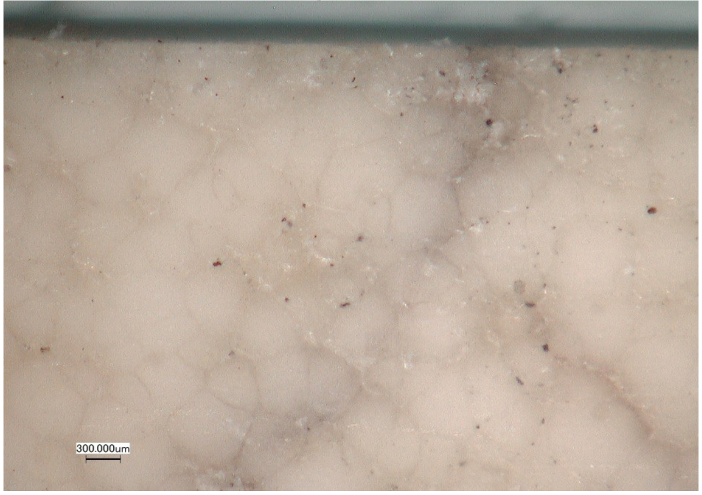

Figure 5

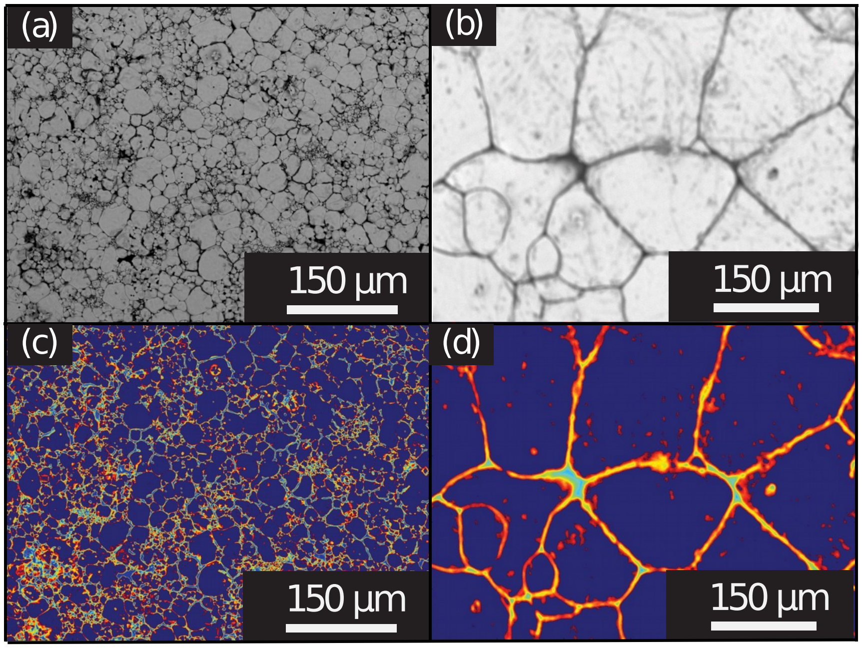

Figure 6

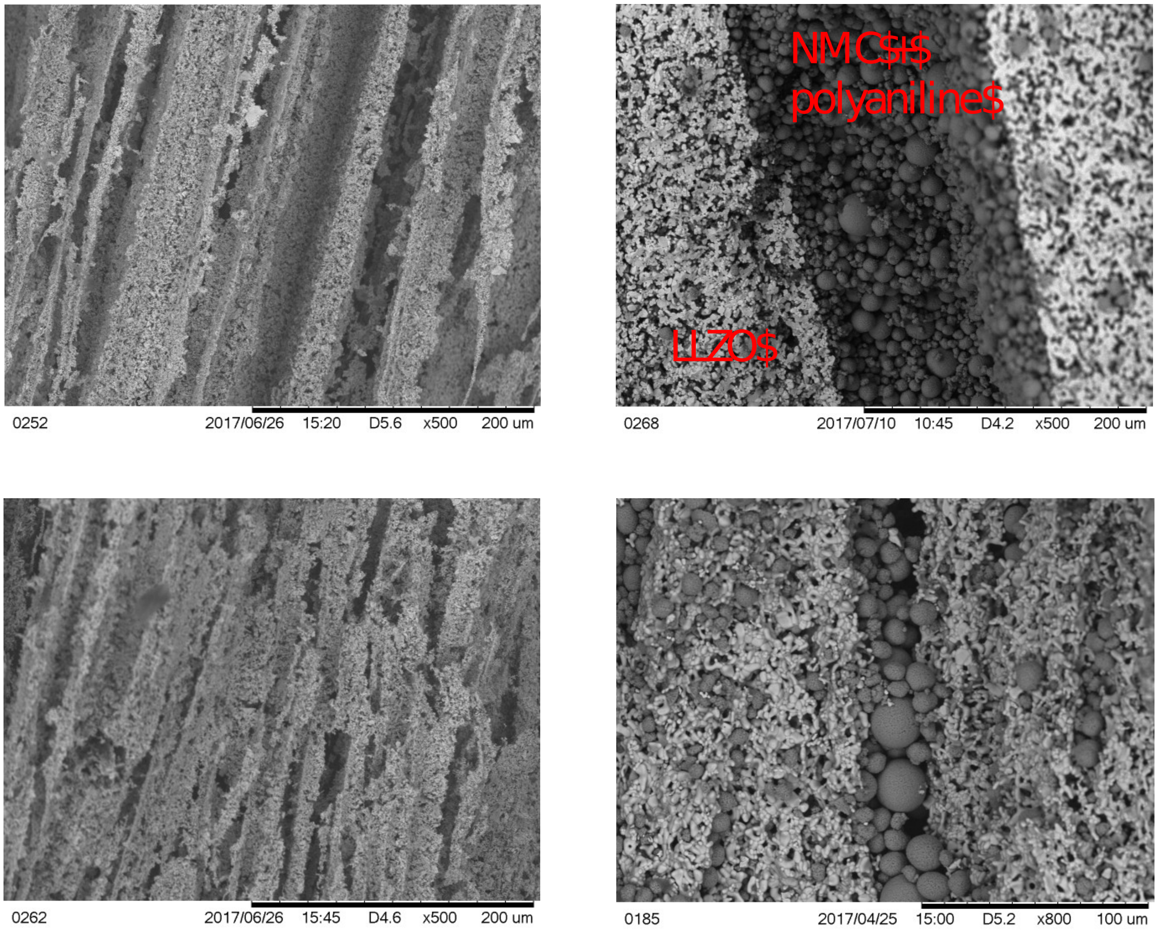
0252
2017/06/26 15:20 D5.6 x500 200 um
NMC$+$
polyaniline$
LLZO$
0268
2017/07/10 10:45 D4.2 x500 200 um
0262
2017/06/26 15:45 D4.6 x500 200 um
0185
2017/04/25 15:00 D5.2 x800 100 um

Figure 7.

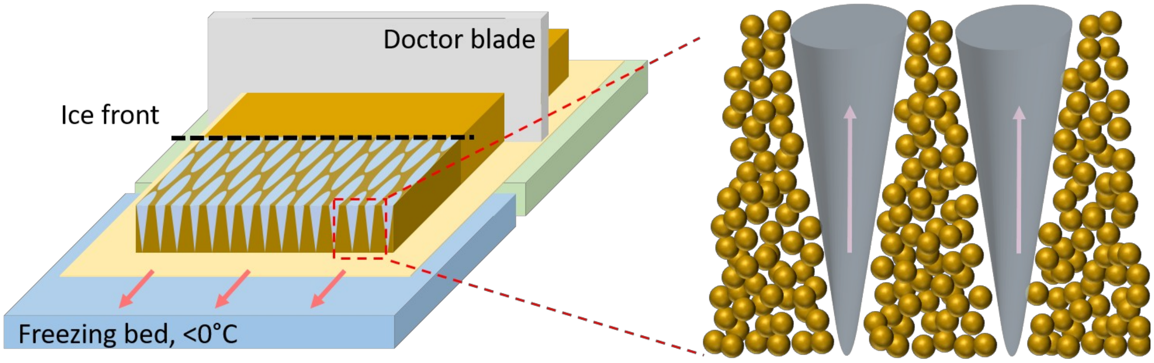
Doctor blade
Ice front
Freezing bed, <0°C

Figure 8

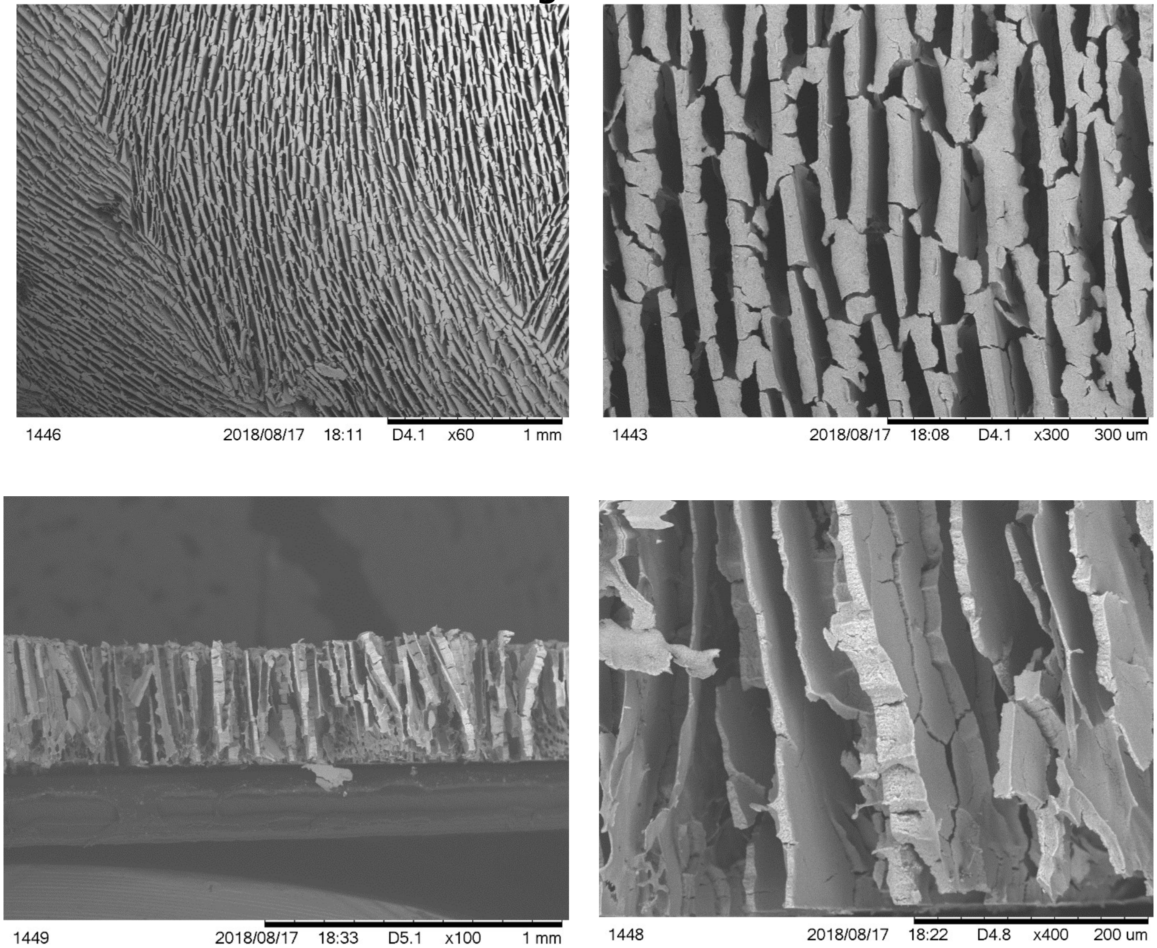
1446 2018/08/17 18:11 D4.1 x60 1 mm
1443 2018/08/17 18:08 D4.1 x300 300 um
1449 2018/08/17 18:33 D5.1 x100 1 mm
1448 2018/08/17 18:22 D4.8 x400 200 um

Figure 9

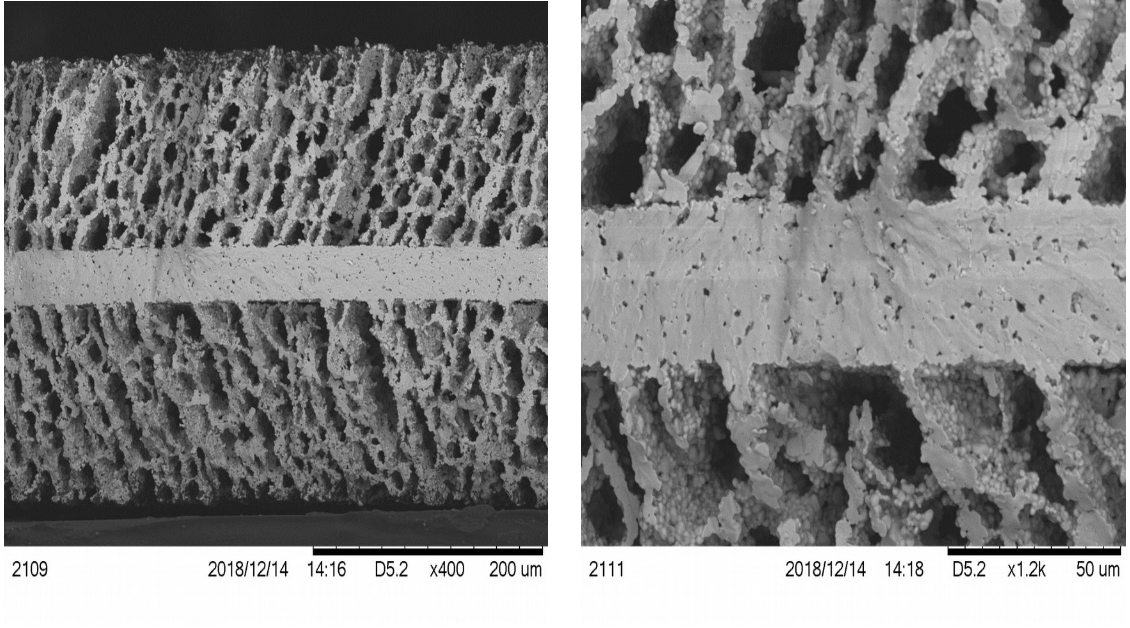
2109
2018/12/14
14:16
D5.2
x400
200 um
2111
2018/12/14
14:18
D5.2
x1.2k
50 um

Figure 10.

Table 1. Properties of Solid Electrolytes

Material	R. T. ionic Conductivity	Processability	Thermal Stability	Stability vs. Li	Moisture Stability	4V stability	Li transference number	Shear modulus
Polymers (e.g. PEO)	Low	Excellent	Moderate	Moderate	Moderate	Poor	Poor	Poor
Sulfides (LGPS, glasses)	V. High	Moderate	Excellent	Moderate	Poor	Poor to Moderate	Excellent	Moderate
LLZO	Moderate	Poor	Excellent	Good	Moderate	Excellent	Excellent	Excellent
LATP	High	Poor	Excellent	Poor	Moderate	Excellent	Excellent	Excellent